Microporous and Mesoporous Materials 271 (2018) 23–32

Contents lists available at ScienceDirect

Microporous and Mesoporous Materials

journal homepage: www.elsevier.com/locate/micromeso

A combined strategy of acid-assisted polymerization and solid state activation to synthesize functionalized nanoporous activated biocarbons from biomass for CO_2 capture

Gurwinder Singh[a,b], Kripal S. Lakhi[d,**], Kavitha Ramadass[d], Sungho Kim[d], Declan Stockdale[c], Ajayan Vinu[d,*]

[a] Future Industries Institute, Division of Information Technology, Engineering and Environment, University of South Australia, Mawson Lakes, South Australia, 5095, Australia
[b] Cooperative Research Centre for Contamination Assessment and Remediation of the Environment, University of South Australia, Mawson Lakes, South Australia, 5095, Australia
[c] School of Mathematical and Physical Sciences, Faculty of Science, University of Technology, Sydney, New South Wales, 2007, Australia
[d] Global Innovative Center for Advanced Nanomaterials, Faculty of Engineering and Built Environment, The University of Newcastle, Callaghan, New South Wales, 2308, Australia

ARTICLE INFO

Keywords:
Arundo donax
Porous
Activated biocarbons
High surface area
CO_2 capture

ABSTRACT

Novel acid treated porous activated biocarbons (APABs) are synthesized from biomass waste, *Arundo donax,* through sulphuric acid polymerization followed by a single step solid state activation using KOH at a fixed carbonization temperature of 600 °C. The specific surface area and the pore volume of the prepared materials is controlled by varying the ratio of KOH to biomass from 1 to 4. The sample prepared with the KOH/biomass ratio of 3 is found to be the best as it exhibits the specific surface area of 2232 $m^2 g^{-1}$ and a pore volume of 1.01 $cm^3 g^{-1}$ which is much higher than those of other samples prepared in this study. Interestingly, XPS and FT-IR studies confirm the presence of oxygen rich functional groups on the surface of the samples, which play an important role in enhancing the CO_2 capture performance of the materials. Among the samples studied, the sample with the highest specific BET surface area exhibits the highest CO_2 adsorption capacity of 21.2 mmol g^{-1} at 0 °C and 30 bar and a moderately high value of 4.1 mmol g^{-1} at 0 °C and 1 bar. The high CO_2 adsorption capacity is attributed to the presence of excellent textural parameters coupled with high micropore volume and the oxygen functional groups. The samples are highly stable and do not show any change in the adsorption capacity even after repeated adsorption experiments. The combination of high adsorption capacity, stability and low cost makes these materials as a potential alternative to other expensive commercially available CO_2 adsorbents.

1. Introduction

Carbon dioxide is widely regarded as the main pollutant for the greenhouse effect and its continuous addition to the environment has raised serious environmental concerns all over the world [1]. The pre- and post-combustion emissions of CO_2 in the flue gas streams of industrial power plants presents a major challenge as it is extremely detrimental to the environment due to its role on global warming [2]. Therefore, there is an urgent demand for the development of cost effective and sustainable technologies to counter and minimize the release of CO_2 to the environment. Carbon capture and storage (CCS) is considered as a promising technology for this purpose. Among the popular methods, liquid amine-based adsorption has been widely employed in industry for capturing CO_2 due to the presence of chemical functional groups on their surface which results in enhanced selectivity. However, it suffers a major drawback in terms of very high energy consumption for material regeneration. As an alternative, adsorption based CO_2 capture using porous carbonaceous materials has gained much interest owing to their inherent properties such as high thermal and chemical stability, large surface areas, high pore volumes and controlled porosity which are critical factors that promote CO_2 adsorption capacities [3,4].

In the published literature, different types of porous materials such as porous organic polymers, hybrid polymers, mesoporous silica, amine

* Corresponding author.
** Corresponding author.
E-mail address: ajayan.vinu@newcastle.edu.au (A. Vinu).

https://doi.org/10.1016/j.micromeso.2018.05.035
Received 9 March 2018; Received in revised form 8 May 2018; Accepted 25 May 2018
Available online 26 May 2018
1387-1811/ Crown Copyright © 2018 Published by Elsevier Inc. All rights reserved.

functionalized mesoporous silica, metal organic framework (MOF), mesoporous carbon, mesoporous carbon nitride and various amine functionalized materials have been proposed for various applications including adsorption, catalysis and CO_2 capture [5–15]. Although the CO_2 capture performance of some of these materials is outstanding, they suffer from major drawbacks such as the use of expensive and hazardous precursors coupled with complex multi-step synthesis procedures and difficult waste disposal procedures which limit the prospects of these materials as industrial scale adsorbents for CO_2 capture. Recent reports have indicated that high microporosity, specific BET surface area and large pore volume are the key parameters for any CO_2 adsorbent [16,17]. There are several ways to enhance these parameters. Chemical activation of porous materials using the activating agents such as KOH, $ZnCl_2$, H_3PO_4 and H_2O_2 one of the unique strategies that offers an attractive method for the enhancement of surface area. Among these, KOH is the leading choice for the purpose owing to its ability to generate high surface areas and create a hierarchical microporous structure within the framework of the activated biocarbons.

Additionally, from an economic point of view, the overall cost of CO_2 capture could be reduced significantly by using inexpensive or freely available carbon precursors and minimizing the number of steps involved in the synthesis procedure. Among the freely available carbon precursors, naturally occurring biomass presents an attractive proposition for use as a starting material for the synthesis of porous carbon materials on a large scale as it is a highly renewable, economically sustainable material and available in abundant quantities in nature [18,19]. The production of activated biocarbons from natural biomass has been the interest of intensive study by many research groups in the recent past [20]. Activated biocarbons produced from biomass possesses high surface area, enhanced porous structure, and good thermal stability which makes them a highly efficient candidate for various applications such as soil and water remediation, lithium batteries, supercapacitors, CO_2 capture etc. [21–28].

Conventionally, activated biocarbons from biomass are produced by a two-step process where a carbon precursor is first pyrolyzed at a certain temperature and then subjected to activation. Hydrothermal carbonization (HTC) of biomass is one alternative to conventional pyrolysis technique, wherein the biomass is subjected to high pressure heat treatment prior to activation [29–31]. This heat treatment helps the formation of levoglucosan and furan-based intermediates which result in the development of aromatic network with a high carbon content and oxygen containing functional groups [29,32]. HTC process is usually performed in an autoclave [20,26,33] and high pressures developed during the whole process could pose serious dangers. In this work, we have proposed a simple, yet novel method based on acidic dehydration of biomass under ambient conditions thereby completely avoiding the use of expensive and operationally difficult high-pressure autoclaving step for the polymerization. We refer to this process as Polymerization-Activation-Carbonization (PAC). In this process, biomass is converted into a carbon rich product using H_2SO_4 dehydration which is then activated using KOH at a mild temperature of 600 °C. The resultant materials show greater porosity and enhanced specific surface area as compared to the non-activated materials. Further, this work demonstrates that highly efficient activated biocarbons are synthesized from a low-cost starting precursor biomass, *Arundo donax,* a perennial grass with a fast growing rate and ability to adapt in different conditions [34]. It may be mentioned here that recently we reported the synthesis of activated biocarbons by direct solid state KOH activation of *Arundo donax* without the acidic dehydration step which resulted in a specific BET surface area of 1122 $m^2 g^{-1}$ and a corresponding CO_2 adsorption capacity of 15.4 mmol g^{-1} at 30 bar and 273 K [35]. The use of H_2SO_4 assisted dehydration of biomass before the solid-state KOH activation step highlights the role of H_2SO_4 in enhancing the final specific BET surface area of the activated biocarbons from 1122 $m^2 g^{-1}$ to 2232 $m^2 g^{-1}$ and a corresponding increase in CO_2 adsorption capacity from 15.4 mmol g^{-1} to 21.2 mmol g^{-1} at 273 K and 30 bar. The enhanced CO_2 adsorption performance of materials in this work could be attributed to the generation of a high surface area and a wide variety of oxygenated functional groups during the KOH activation step with the latter imparting a negative charge on the surface that helps in improving the adsorption of CO_2. Based on our experimental results, it is proposed that the acid treatment step not only cross-links all the carbon components and creates functional groups through oxidation and dehydration but also dissolves the inherent inorganic metallic constituents present in the biomass. We believe that the procedure reported in this work could provide a facile and economically viable method of converting waste biomass such as *Arundo donax* into potential large-scale environmental friendly and economical commercial adsorbents for CO_2 capture.

2. Experimental section

2.1. Preparation of acid treated porous activated biocarbons (APABs)

Arundo donax was used as a source of biomass in the preparation of acid treated porous activated biocarbon materials. In a typical synthesis, 5 g of powdered biomass, 10 ml millique water and 2.24 ml sulphuric acid were mixed together and placed in a hot air oven at 100 °C for 6 h after which the temperature was increased to 160 °C and maintained for another 6 h. This treatment was chosen to completely remove any moisture and dissolvable inorganic metallic species present in the parent biomass. The obtained charred material was grinded to fine powder and the resulting powder samples was labelled as AB (acid treated biocarbon). Subsequently, AB was then impregnated with different amounts of solid KOH (varying the ratio of AB to KOH from 1 to 4). The resulting mixture containing KOH was carbonized for 2 h at 600 °C in a horizontal tube furnace connected to a continuous supply of nitrogen. The carbon materials were cooled down to 25 °C and washed thoroughly first with 1 M HCl solution followed by washing with millique water to remove all the inorganic and metallic residues. The washed materials were completely dried at 100 °C for overnight. The final obtained porous materials are named as APAB-n, where APAB is abbreviated as acid treated porous activated biocarbons and n denotes the ratio of KOH/APAB. For example, APAB-1 was prepared using KOH/APAB ratio of 1 and then carbonized at a temperature of 600 °C. For comparison, biomass was also pyrolyzed at 600 °C without acid treatment and activation and denoted as B.

2.2. Physico-chemical characterisation of APABs

The specific BET surface area and other textural parameters were obtained from nitrogen sorption isotherms recorded at 77 K using Micromeritics ASAP 2420 instrument. Prior to analysis, samples were degassed overnight at 250 °C under vacuum. Specific surface area (SA_{BET}) was measured using BET (Brunauer Emmett-Teller) equation at a relative pressure range of *p/po* 0.05–0.20 and total pore volume was taken at *p/po* = 0.99. Total micropore area, external surface area and micropore volume were determined using t-plot method. XRD diffraction patterns were obtained using PANalytical Empyrean instrument for examining the crystal structure of all the materials. The samples were put at the centre of a circular holder and then irradiated with $CuK\alpha_1$ and $K\alpha_2$ radiation (λ = 1.5406 Å and 1.5444 Å) produced at an operating voltage of 40 kV and a current of 40 mA. Wide angle XRD patterns were recorded over the range of 2θ = 10–80° under a continuous scan mode using 0.06° as step size. Scanning electron micrographs were recorded on Zeiss merlin scanning electron microscope using an operating voltage of 2 kV. Surface functional groups were investigated using FTIR spectroscopy technique on a Newport FTIR spectrometer. A reference carbon material was used to set up a background spectrum every 30 min and then the sample was analysed under infrared region from 4000 cm^{-1} to 400 cm^{-1} using 8 cm^{-1} resolution. X-ray photoelectron spectroscopic measurements were measured using Kratos Axis

ULTRA X-ray photoelectron spectrometer. A monochromatic Al K_α X-rays source of incident radiation operating at 225 W, 15 kV and 15 mA was used. The samples were outgassed under vacuum for 12 h before the actual measurements. Survey spectra were recorded by employing a pass energy of 160 eV, binding energy range between 1200 and 0 eV with 1.0 eV step and a dwell time of 100 ms. High resolution spectra were recorded at a pass energy of 20 eV.

2.3. CO_2 uptake measurements

Quantachrome Isorb HP1 instrument fitted with an external water circulator to control the temperature was employed for recording high pressure CO_2 adsorption isotherms. Prior to analysis, a measured quantity of analysis samples was outgassed for 12 h at temperature of 250 °C under vacuum. The analysis samples were then individually subjected to CO_2 adsorption measurements in a high-pressure cell. CO_2 adsorption isotherms for each analysed sample were obtained at three different analysis temperatures of 0 °C, 10 °C and 25 °C and a pressure range from 0 to 30 bar. The isoelectric heat of adsorption for the samples was calculated using Clausius - Clapeyron equation to determine the nature of interactions between adsorbents, APABs and adsorbate CO_2. The isosteric heat of adsorption was calculated using the isotherms recorded at 0, 10 and 25 °C.

3. Results and discussion

3.1. X-ray diffraction (XRD) analysis

Fig. 1 shows the XRD patterns of **APABs** synthesized using different amounts of impregnation with KOH. All samples display two broad peaks at 2θ = 22–23° and 2θ = 43–44° corresponding to (002) and (101) reflection planes indicating the presence of a disordered carbon structure [36,37]. It is to be noted that the samples synthesized using the lowest and the highest impregnation ratios of KOH/biomass (1 and 4) show relatively narrower intensities for the peak occurring at 2θ = 22–23° as compared to the samples prepared using KOH impregnation ratios of 2 and 3. This could be ascribed to the greater amount of crystallinity in the samples arising due to insufficient and extensive reaction of the KOH with the biomass carbon, respectively. On the other hand, samples prepared with KOH impregnation ratios of 2 and 3 have just the right amount of KOH required for the chemical reaction with biomass carbon which eventually results in the formation of disordered biocarbon and show broad XRD peaks. This combination is favorable as the formation of highly disordered and randomly oriented graphitic carbon layers generate higher specific surface areas which is an essential requirement for obtaining high CO_2 adsorption capacities [38]. Further, a slight shift in the peak positions for both the low (2θ = 22°–23°) and high angles (2θ = 43°–44°) is observed when the KOH impregnation ratio is increased from 1 to 4. The XRD of non-activated samples was also compared as shown in Fig. S1. Biochar (B) obtained from parent biomass shows the presence of sharp peaks of sylvite (KCl). Acid treated biocarbon (AB) shows some residual impurity peaks whose intensity decreases after carbonization process (APAB-0). Based on the above analysis, it can be concluded that the graphitization of the biomass carbon is only possible after chemical activation with KOH which results in the formation of porous activated biocarbons [39].

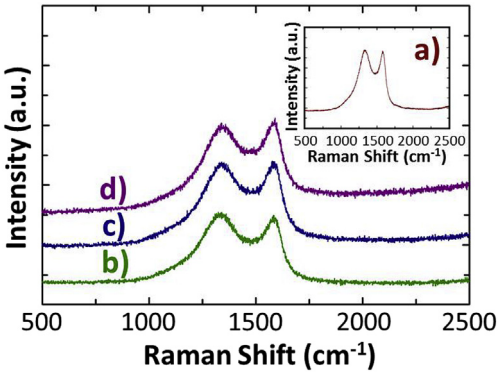

Fig. 2. Raman spectra of a) APAB-1, b) APAB-2, c) APAB-3 and d) APAB-4.

The graphitization degree of the synthesized APAB materials was further investigated using Raman spectroscopy and the results are depicted in Fig. 2. A pure crystal of graphite exhibits an intense Raman shift (G band) around the position of 1575 cm^{-1} whereas an additional Raman shift (D band) is also detected in case of materials that contain poorly graphitized structures [40]. As expected, similar type of spectra containing both D and G bands was observed for all the synthesized

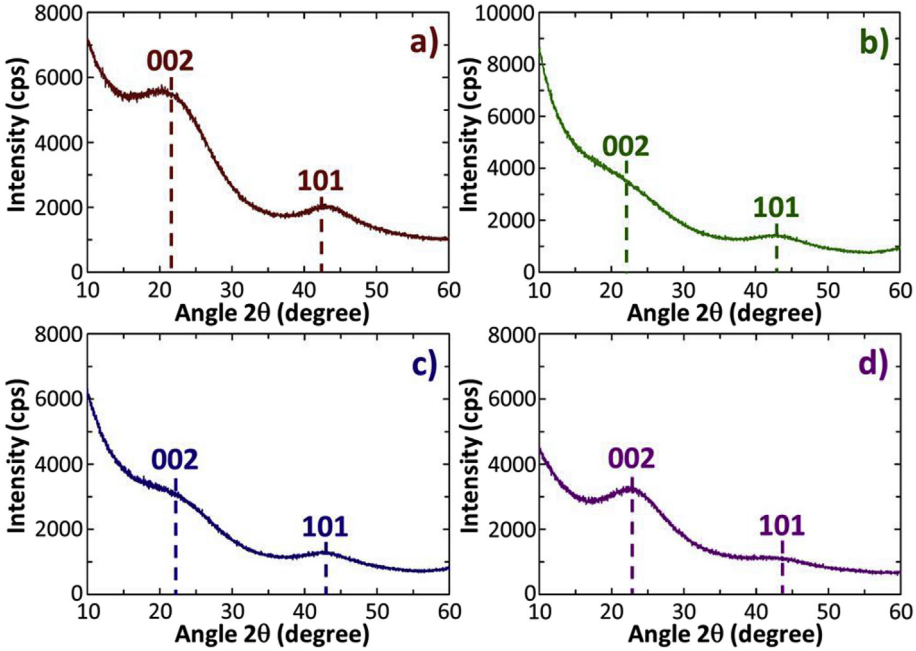

Fig. 1. XRD patterns of a) APAB-1, b) APAB-2, c) APAB-3 and d) APAB-4.

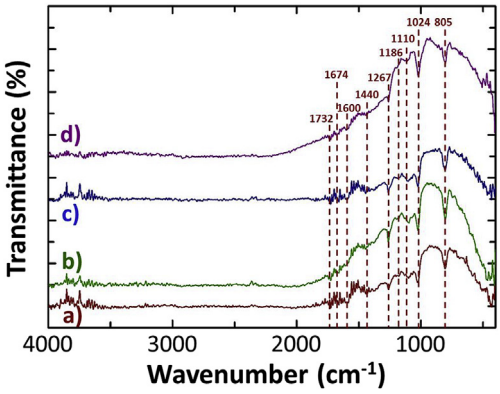

Fig. 3. FT-IR spectra of a) APAB-1, b) APAB-2, c) APAB-3 and d) APAB-4.

APAB materials which is indicative of their amorphous nature and aligns with the XRD observations. The degree of disorder as calculated from the ratio of intensities of G (I_G) and D (I_D) band for the activated biocarbons varied in the order of APAB-4 (1.03) > APAB-3 (1.01) > APAB-2 (1.00) > APAB-1 (0.98). This indicates that KOH plays an important role in controlling the number of graphitic domains generated in the structure of activated biocarbon during the process of carbonization and activation. The higher impregnation amounts of the activating agent resulted in the formation of more disorderly graphitic structures and vice versa.

3.2. Fourier transform infra-red (FTIR) spectra analysis

The presence of carbon and oxygen as the main functional elements was confirmed by the FTIR characterization of the activated samples where a number of different peaks were observed **(**Fig. 3**)**. As can been seen, all the samples show the peaks of similar functional groups with different intensity. Three prominent peaks occurring at 805 cm^{-1}, 1024 cm^{-1} and 1267 cm^{-1} corresponding to a substituted benzene ring, = C – O – C stretching in aromatic ether or 2H - chromene and 4H-chromene like systems, in plane O—H bending in carboxylic acid or asymmetric = C – O – C stretching vibrations in 2H - chromene, 4H - chromene and 2 - pyrone systems, respectively [41] could be seen in all the samples. Additionally, six relatively less prominent peaks occurring at 1110 cm^{-1}, 1186 cm^{-1}, 1440 cm^{-1}, 1600 cm^{-1}, 1674 cm^{-1} and 1732 cm^{-1} could also be seen in these samples. These peaks can be attributed to different functional groups as follows; a) ~1110 cm^{-1} stands for in plane C – H bending vibration [42], b) ~1186 cm^{-1} can be assigned to phenolic vibrations [43], c) ~1440 cm^{-1} can be related to C = C skeletal stretching in an aromatic ring [44], d) ~1600 cm^{-1} reveals C = C and C=O stretching vibrations in carboxylic acids [45], e) ~1674 cm^{-1} presents C = O stretching vibrations in ketones [46] and f) ~1732 cm^{-1} indicates a C = O stretching vibration in systems such as carboxylic acids and esters [47]. It can be easily inferred from FT-IR studies that the synthesized APABs are highly aromatic in nature and contain abundant oxygenated functional groups such as phenolic and carboxylic acid groups, which impart a negative charge to the surface of activated biocarbon materials which results in enhancement in the CO_2 adsorption capacities of these materials.

3.3. Scanning electron microscopy (SEM) analysis

Fig. 4 and Fig. S2 show the morphology of the activated and non-activated biocarbons respectively as observed under SEM. All samples including activated and non-activated biocarbons exhibit a disorder morphology which is generally expected for activated biocarbons derived from biomass [48]. Non-activated samples with or without acid treatment (B, AB and APAB-0) show no porosity at all in the biocarbon structures as shown in Fig. S2. This is expected as these three are merely the carbon derived from biomass without any chemical activation and similar results have been reported by various research groups [49]. However, upon chemical activation with KOH, a considerable amount of porosity is introduced in the biocarbon structure (Fig. 4) which is a result of various chemical reactions taking place between biomass carbon and KOH. A generalized reaction occurring between biomass carbon and KOH could be represented as [50].

$$6KOH + C \rightarrow 3H_2 + 2K_2CO_3$$

As can be seen from Fig. 4, APAB-1 shows lesser porosity which increases progressively as the KOH/biomass impregnation ratio increases from 1 to 3. APAB-4 synthesized with the highest KOH/biomass impregnation ratio (4) shows a considerable loss in porosity which is probably caused by destruction of biocarbon structure due to severe chemical effect of KOH. A KOH impregnation ratio of 2 and 3 generates the highest amount of porosity in the biocarbons as these are considered optimal for reactions between biomass carbon and KOH. A wide variety of pores ranging from micropores of size 1–2 μm to mesopores of size 2 - < 10 μm could be observed in Fig. 4b and c. These pores are found in a disordered array of either small or big clusters but occur all over in the biocarbon structure. It is believed that the small micropores are effective in initial capture of CO_2 molecules which can further enter the bigger mesopores and interact with the surface functional groups resulting in high overall CO_2 capture. The porous structure of the synthesized materials was further confirmed using the TEM analysis of the optimized material APAB-3. As shown in Fig. S6, the TEM images reflect the microporous nature of the material and contain a highly disordered distribution of porous structure which is typical of amorphous carbon.

3.4. Nitrogen sorption analysis

Nitrogen sorption measured at a temperature of 77 K was used to quantify the specific surface area and other textural parameters of the APAB-n. Fig. 5 and Fig. S3 show nitrogen adsorption-desorption isotherms of activated biocarbons and non-activated biocarbons respectively and Table 1 summarizes the textural parameters of activated biocarbons. As per Fig. S3, the non-activated biocarbons show little to no N_2 adsorption with unusual shape of the sorption curves which indicates that these are highly non-porous in nature. On the other hand, upon KOH activation, the adsorption of N_2 increases manifolds and the observed shape of the isotherms as shown in Fig. 5 correspond to type – I as per IUPAC classification for microporous materials [51]. A relatively sharp and upward increasing shape of the isotherms at low pressure (P/P_0 = 0.0–0.2) indicates that a large amount of N_2 is adsorbed in the microporous structure of the activated biocarbons [52]. The shape of the hysteresis loops changes progressively as the KOH to biomass ratio increases from 1 to 4. The presence of an H_4 type hysteresis loop within a relative pressure range of 0.45–0.90 suggests the co-existence of both micropores and slit like mesopores in APAB-1 and APAB-2 [53]. Furthermore, APAB-3 shows isotherm belonging to a typical microporous material whereas APAB-4 exhibits a small tail at the higher relative pressure which is attributed to the presence of macropores [54]. These observations are consistent with the textural parameters obtained in Table 1. The lowest surface area of 764 $m^2 g^{-1}$ is observed for sample prepared using the lowest KOH to biomass ratio of 1. Whereas a KOH to biomass ratio of 3 was found to be the optimum ratio for obtaining the highest specific BET surface area of 2232 $m^2 g^{-1}$ and a reasonably large pore volume of 1.0 $cm^3 g^{-1}$. As discussed in earlier section, increasing the KOH impregnation ratio to 4 results in excessive carbon burn off causing partial or complete collapse of the biocarbon structure resulting in specific BET surface area of 1087 $m^2 g^{-1}$ which is almost less than half the specific BET surface of APAB-3 sample. Interestingly, sample APAB-2 has nearly the same surface area as that of APAB-4 and slightly higher than that of APAB-1.

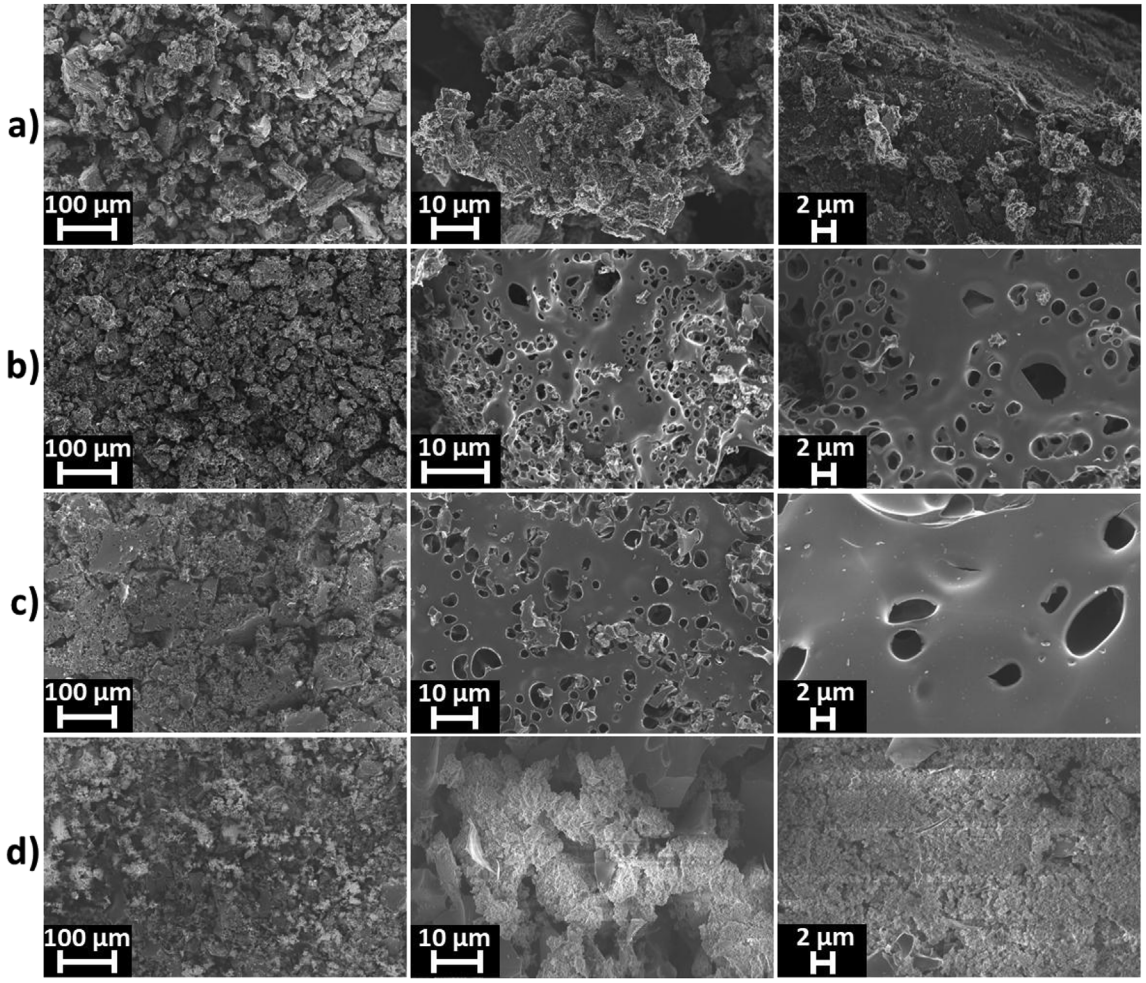

Fig. 4. SEM images taken at different resolution for a) APAB-1, b) APAB-2, c) APAB-3 and d) APAB-4.

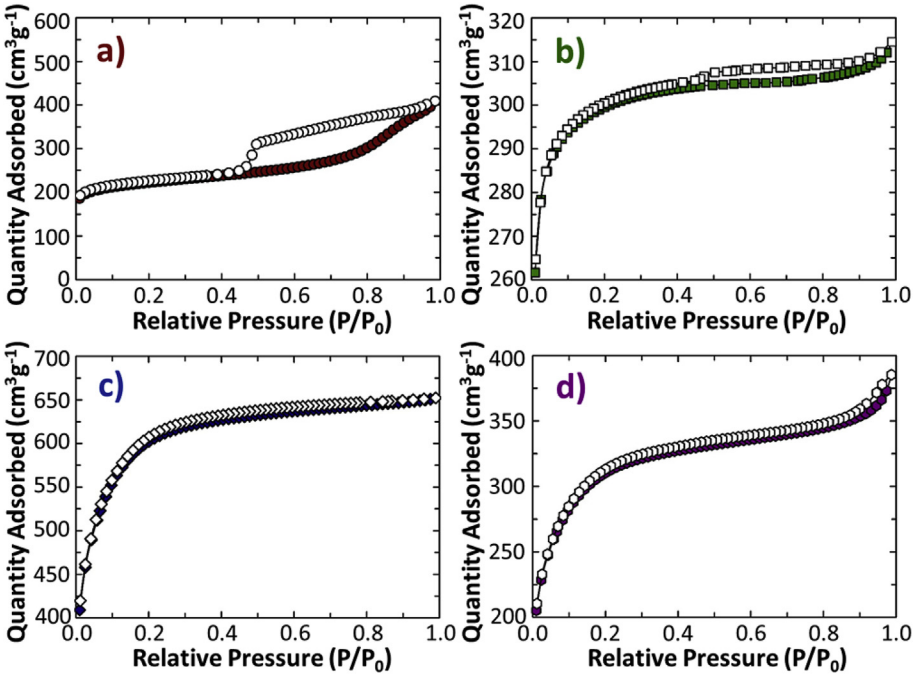

Fig. 5. N_2 adsorption-desorption isotherms of a) APAB-1, b) APAB-2, c) APAB-3 and d) APAB-4.

Table 1
Textural properties of APABs synthesized from *Arundo donax* under different activation conditions.

Sample Code	[a]SSA_{BET} ($m^2\ g^{-1}$)		[c]Pore Volume ($cm^3\ g^{-1}$)		[e]PW (nm)
	Total	[b]% Micro	Total	[d]% Micro	
APAB-1	764	71	0.63	40	0.56
APAB-2	1018	90	0.49	84	0.56
APAB-3	2232	63	1.01	55	0.82
APAB-4	1087	55	0.59	44	0.82

[a] BET surface area.
[b] Percentage of Micropore surface area.
[c] Total pore volume.
[d] Percentage of Micropore volume.
[e] Pore width calculated using MP method.

This trend suggests that it is important to mix optimum quantity of KOH with biochar to get the highest possible specific surface area; all other factors remaining same.

In our recent work, we demonstrated that activated biocarbons prepared without any acid treatment but under similar synthesis conditions as sample APAB-3 in this study shows a relatively lesser surfacer area of 849 $m^2\ g^{-1}$ [30]. The difference in the surface area reveals the crucial role played by the acid treatment step before activation with solid KOH. The superior textural parameters of APAB-3 could be explained based on the strong dehydrating effect of sulphuric acid which removes a lot of inorganic impurities and catalyses the polymerization of carbon prior to KOH activation and aids in the production of materials with superior textural properties and functional moieties. Fig. 6 shows pore size distributions of all activated biocarbons calculated using MP method. As AB and APAB-0 samples do not show any significant pore volume or pore size distribution as calculated using MP method, it could be easily concluded that these samples have practically no porosity or the samples are predominantly non-porous for all practical purpose. On the other hand, activated biocarbons show a reasonably narrow pore size distribution as shown in Fig. 6. Further, samples APAB-1 and APAB-2 show almost a similar type of pore size distribution centred on 0.56 nm which can be classified as ultramicropores (< 0.8 nm). The remaining two samples of APAB-3 and APAB-4 show a slightly higher pore size of 0.82 nm.

3.5. X-ray photoelectron spectroscopy (XPS) analysis

All activated and non-activated biocarbons were analyzed by using XPS analysis for determining the surface elemental composition and to study the nature and bonding characteristics of different types of carbon and oxygen species. Fig. S4 A) and B) shows the XPS survey spectra for activated and non-activated biocarbons, respectively. Based on the survey spectra, the surface composition of all the samples is found to be predominantly carbon with traces of other impurities and a rich distribution of oxygen on the surface. As per the XPS elemental composition summarized in Table 2, all samples possess surface carbon content in the range of 71–87% except APAB-4 which shows a significantly reduced carbon content of 39%. This again confirms that a very high impregnation ratio of KOH to biomass carbon results in excessive carbon burn off and consequently the surface gets oxidized to a much greater extent as compared to other samples prepared with lower KOH impregnation ratio. The acid treated sample AB shows a lesser carbon content of 71% but upon activation and carbonization, the carbon content of all biocarbons increases and is found to be in the range of 85–87%. All materials are found to possess a high amount of oxygen on the surface (11.2–43.5%) which is acquired as follows; the non-activated/non-carbonized sample AB shows higher amount of oxygen (26%) which could have come from the acid treatment while the activated/carbonized samples, except for APAB-4 which is mostly oxidized, shows relatively lesser oxygen content due to losses of oxygen functional groups during carbonization. The chemical structure of carbon and oxygen in all samples was further probed using high resolution scans.

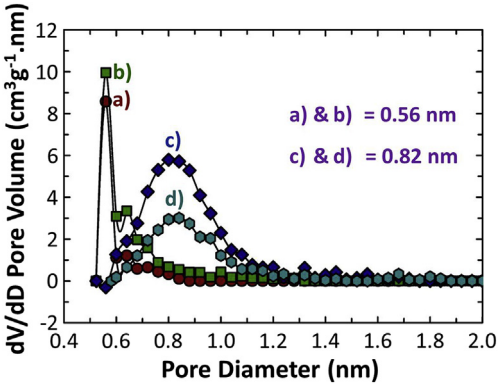

Fig. 6. Pore size distribution calculated using MP-method of a) APAB-1, b) APAB-2, c) APAB-3 and d) APAB-4.

Table 2
XPS elemental composition of all the synthesized biocarbon materials.

Sample code	Carbon (%)	Nitrogen (%)	Oxygen (%)
AB	71	0.62	26.0
APAB-0	87	0.92	11.2
APAB-1	85	0.80	13.1
APAB-2	86	0.39	13.3
APAB-3	87	0.56	11.5
APAB-4	39	0.61	43.5

Fig. 7 and Fig. S5 show the high resolution C1s and O1s spectra for activated and non-activated biocarbons, respectively. The C1s XPS spectra of activated biocarbons (Fig. 7) can be fitted into one main peak representing graphitic carbon (B.E. 284–284.1 eV) accompanied by two smaller peaks corresponding to phenolic -C-O (B.E. 285.5–285.7 eV) and -O-C=O (B.E. 288.0–288.1 eV) groups, respectively [55,56]. In case of AB (Fig. S5) and APAB-4, there is a peak appearing for carbonate type functionality around B.E. of ~281 eV. It is to be pointed out that it is a challenge to characterize the high resolution C1s peaks of non-activated materials as biomass carbon might be associated with the inherent constituents present in the biomass. The deconvoluted O1s high resolution XPS spectra of the activated and non-activated biocarbons can be approximately fitted into two main peaks corresponding to carbonyl -C=O (B.E. 530.7–531 eV) and ethereal type -O-C-O (B.E. 532.1–532.4 eV) groups [57,58]. However, in case of acid treated sample AB, the O1s high resolution spectra show a peak at a relatively low B.E. of 529.1 eV which could be due to the presence of impurities. The presence of all these different types of oxygenated functional groups imparts a negative charge or basic character to the surface of activated biocarbons which helps to anchor the slightly acidic CO_2 molecules through acid base interactions. Based on the XPS analysis, it can be concluded that the surface of activated biocarbons is highly functionalized with oxygenated functional groups sourced from the biomass and the activating agent during the process of carbonization.

3.6. CO_2 capture analysis

The chemical activation of biomass carbon with KOH results in enhanced specific surface area and micropore volume of the synthesized activated biocarbons. These features make the activated biocarbons suitable for applications such as gas adsorption wherein surface area and pore volume play a crucial role. The activated biocarbons prepared in this work were used as adsorbents for high pressure CO_2 capture under different analysis conditions and pressure up to 30 bar.

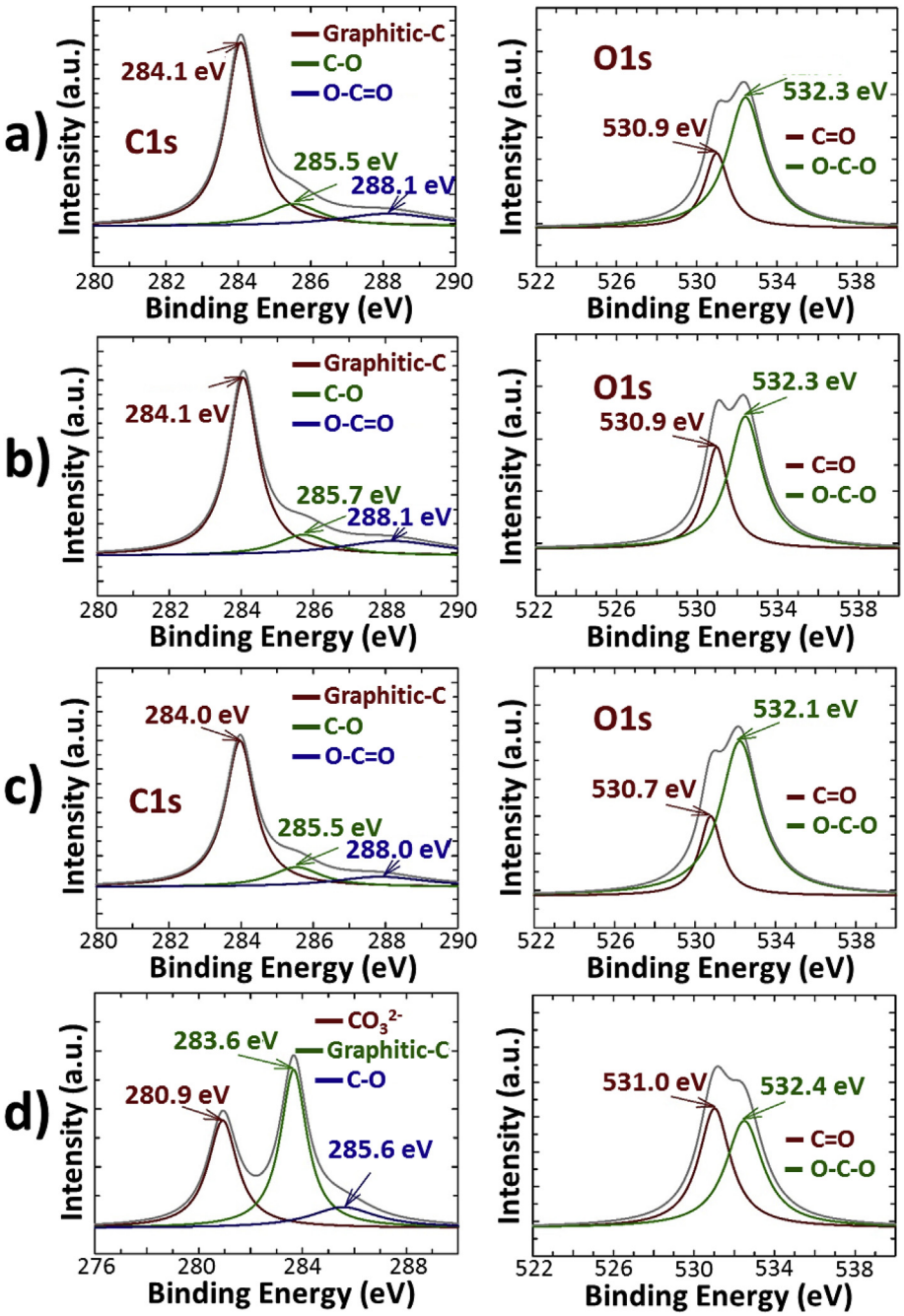

Fig. 7. High resolution C1s and O1s XPS spectra of a) APAB-1, b) APAB-2, c) APAB-3 and d) APAB-4.

Among the samples prepared, APAB-1 and APAB-3 with the lowest and the highest specific BET surface areas were used for CO_2 adsorption. Fig. 8 shows the comparison of CO_2 adsorption isotherms for these samples at 0 °C. It can be clearly seen that there is a direct correlation between surface area of the materials and their respective CO_2 uptake under the same analysis conditions. The effect of analysis temperature on CO_2 adsorption capacity was also demonstrated for the best sample APAB-3. Fig. 9 shows the CO_2 adsorption isotherms recorded for APAB-3 sample at three different analysis temperatures of 0 °C, 10 °C and 25 °C and a pressure up to 30 bar. Table 3 summarizes the adsorption capacities of APAB-3 under different analysis conditions. The low and high-pressure CO_2 adsorption conditions closely mimic the post combustion and pre-combustion capture of CO_2 from flue gas streams. It can be seen from Fig. 9 that the CO_2 adsorption capacity of APAB-3 at all the three analysis temperatures exhibits a strictly increasing trend in the pressure range 0–5 bar and at a low-pressure range of 0–2 bar. The CO_2 adsorption capacities observed at 0 °C/1 bar and 0 °C/30 bar are 4.1 mmol g^{-1} and 21.2 mmol g^{-1}, respectively. On the other hand, as expected, at a temperature of 10 °C, the CO_2 adsorption capacity reduces slightly as compared to that at 0 °C measuring about 3.3 mmol g^{-1} at 1 bar and 19.4 mmol g^{-1} at 30 bar. With further increase in temperature to 25 °C, CO_2 adsorption capacity furthers decreases to 3.2 mmol g^{-1} at 1 bar and 17.4 mmol g^{-1} at 30 bar.

The variation of CO_2 adsorption capacity with temperature is well reported in literature and is attributed to the exothermic nature of the CO_2 adsorption process [59]. At low temperatures, the adsorption phenomenon is physisorption in nature and the interactive forces are strong, however, as the temperature is increased, the kinetic energy of the molecules increases and consequently the strength of the Vander Wall forces decreases resulting in reduced attraction between adsorbent

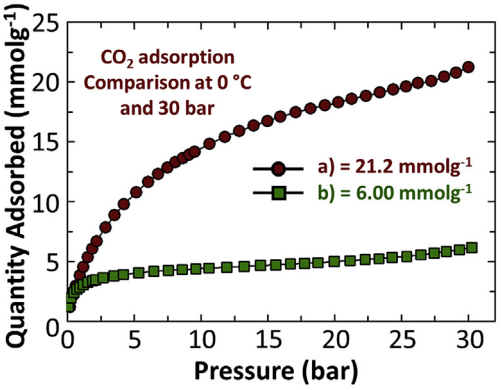

Fig. 8. The comparison of the high-pressure CO_2 adsorption isotherms measured at a temperature of 0 °C and pressure range of 1–30 bar over a) APAB-1 and b) APAB-3.

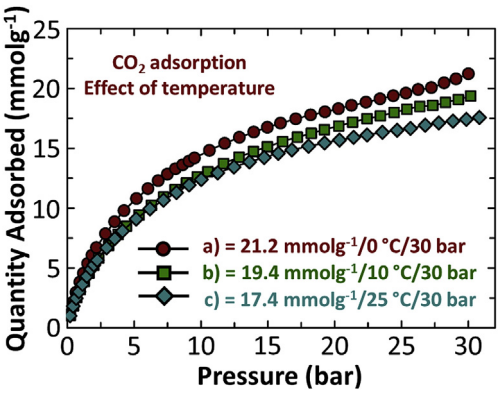
CO2 adsorption
Effect of temperature
a) = 21.2 mmolg-1/0 °C/30 bar
b) = 19.4 mmolg-1/10 °C/30 bar
c) = 17.4 mmolg-1/25 °C/30 bar
Quantity Adsorbed (mmolg-1)
Pressure (bar)

Fig. 9. The comparison of high-pressure CO_2 adsorption isotherms measured over APAB-3 at three different temperatures a) 0 °C and b) 10 °C and c) 25 °C.

Table 3
CO_2 uptakes over optimized material APAB-3.

Temperature (°C)	Pressure (bar)	CO_2 uptake (mmol g^{-1})
0 °C	1	4.1
	15	16.7
	30	21.2
10 °C	1	3.3
	15	15.1
	30	19.4
25 °C	1	3.2
	15	14.2
	30	17.4

and adsorbate molecules which explains lower CO_2 adsorption at higher analysis temperature. These observations are in accordance with the Le Chatelier's principle. Based on the shape of the isotherms, it can be said that a further increase in pressure would result in higher adsorption. This is an interesting phenomenon as the high-pressure conditions are similar to those encountered in the separation of CO_2 from natural gas. It is also worthwhile to mention that the CO_2 adsorption capacity of 21.2 mmol g^{-1} is much higher than what we have reported previously (15.4 mmol g^{-1}) where the KOH activated biocarbons were synthesized without acid treatment step [30]. The difference in the CO_2 adsorption performance be explained by the effect of acid treatment step which not only offers a large number of oxygen functional groups through the polymerization of the carbon components but also removes most of the inorganic impurities such as Sylvite. This supports a change in the surface charge of the adsorbents as well as the enhancement in the specific surface area of the adsorbents. The CO_2 adsorption capacities

Table 4
Comparison of CO_2 uptake over biomass and non-biomass based materials at 0 °C.

Carbon source	CO_2 uptake at 0 °C (mmol g^{-1})		Ref.
Arundo donax	4.1/1 bar	21.2/30 bar	This work
Palm fruit bunch	1.3/1 bar	–	[62]
Coconut shell	3.7/1 bar	–	[63]
African palm stones	3.7/1 bar	–	[63]
Ligand incorporated MOF	1.6/1 bar	–	[64]
Mesoporous carbon nitride		15.4//30 bar	[65]
Seaweed	2.4/1 bar	–	[66]
Zeolite 13X	–	7.3/32 bar	[67]
MOF-5	–	22/40 bar	[68]
Arundo donax	4.8/1 bar	14.1/30 bar	[69]

observed are quite high when compared to other biomass and non-biomass derived materials reported in the previous literature as shown in Table 4 and this again highlights the significance of our work. Additionally, the same material was reused again and over for measuring the adsorption isotherms shown in Fig. 9 which is indicative of the reusability of the synthesized materials. Overall, in this work, we have proposed a relatively inexpensive and reliable method for the synthesis of APAB carbons with a specific surface area as high as 2232 $m^2 g^{-1}$ and a pore volume of 1.01 $cm^3 g^{-1}$. This makes these materials highly suitable adsorbents for CO_2 capture operations at both low and high-pressure conditions.

3.7. Isoelectric heat of adsorption

Isoelectric heat of adsorption is an indicative of the strength of interaction between adsorbate and adsorbent in the adsorption process. The isosteric heat of adsorption for the best samples APAB-3 is shown in Fig. 10 which was calculated using the isotherms obtained at three temperatures 0 °C, 10 °C and 25° C. The isosteric heat of adsorption is low for APAB-3 sample lying in the range 5–15 kJ mol^{-1} which indicates that the nature of the interactions between APAB-3 sample and CO_2 molecules is purely physical in nature [60]. Furthermore, the isosteric heat of adsorption shows a decreasing trend with increasing CO_2 loading which suggests that the surface is heterogeneous in nature and this trend is very well reported in literature [61]. This phenomenon could be explained as follows: at low pressures, the incoming CO_2 molecules are strongly adsorbed on the isolated and freely available sites on the surface of the material resulting in higher isoelectric heat of adsorption of 15.4 kJ mol^{-1}. As the CO_2 pressure increases, further adsorption of the CO_2 molecules occurs resulting in the formation of a monolayer on the surface of the material. As the pressure is further increased, more CO_2 molecules get adsorbed resulting in complete coverage of the surface and thereby filling up of the pores created due

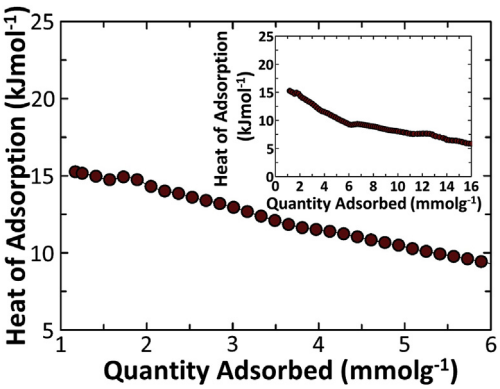

Fig. 10. Isoelectric heat of adsorption of APAB-3 recorded at three different temperatures of 0 °C, 10 °C and 25 °C.

to KOH activation. The multi-layers formed reduces the interaction between incoming CO_2 molecules and the adsorbate surface which is reflected in the low values of heat of adsorption at higher CO_2 loading.

4. Conclusions

Novel acid treated porous activated biocarbon materials with a high specific surface area and a pore volume were derived from waste biomass, *Arundo donax* using a facile synthesis procedure. This strategy not only offers a simple and quick methodology but also employs inexpensive starting carbon source which lowers the overall cost associated with the process. Chemical activation with KOH was found to produce porous carbons with a high specific surface area, high degree of microporosity and graphitization. The optimized sample synthesized using a KOH/biomass impregnation ratio of 3 yielded biocarbon with the highest specific surface area of 2232 $m^2 g^{-1}$ and a pore volume of 1.01 $cm^3 g^{-1}$. The highest CO_2 adsorption capacity for the best sample was found to be 21.2 mmol g^{-1} at 0 °C and under a high pressure of 30 bar and these conditions strongly mimic the adsorption of CO_2 in natural gas operations. The superior CO_2 capture performance of APAB-3 was found to be attributed to the excellent textural parameters of combined with the surface functional groups. We believe that the material and methods presented in this work could be extended for the preparation of series of porous activated biocarbons from different biomasses and will open up a new platform for the design of low-cost adsorbents for various other applications including water treatment and dye adsorption.

Conflicts of interest

There are no conflicts of Interest to declare.

Acknowledgements

The work carried out in this manuscript was financially supported by the Cooperative Research Centre for Contamination Assessment and Remediation of the Environment (CRC CARE) through grant no. (3.3.02-15/16), whose activities are funded by the Australian Government's Cooperative Research Centres Programme. One of the authors acknowledge Prof. Ravi Naidu and Dr. P. Srivastava for providing enough facilities to execute this project and mentoring. A. Vinu also acknowledges the research support and laboratory facilities provided by Future Industries Institute, University of South Australia, (FT100100970) and Australian Research Council for the Future Fellowship and Discovery Grants (DP150104828; DP170104478). Authors also acknolwedge Dr. Dawei Su from University of Technology, Sydney for the Raman measurements.

Appendix A. Supplementary data

Supplementary data related to this article can be found at http://dx.doi.org/10.1016/j.micromeso.2018.05.035.

References

[1] X. Zhao, X. Hu, G. Hu, R. Bai, W. Dai, M. Fan, M. Luo, J. Mater. Chem. A 1 (2013) 6208–6215.
[2] M.R. Benzigar, S.N. Talapaneni, S. Joseph, K. Ramadass, G. Singh, J. Scaranto, U. Ravon, K. Al-Bahily, A. Vinu, Recent advances in functionalized micro and mesoporous carbon materials: synthesis and applications, Chem. Soc. Rev. 47 (2018) 2680–2721.
[3] J. Song, W. Shen, J. Wang, W. Fan, Carbon 69 (2014) 255–263.
[4] L. Xu, L. Guo, G. Hu, J. Chen, X. Hu, S. Wang, W. Dai, M. Fan, RSC Adv. 5 (2015) 37964–37969.
[5] K.S. Lakhi, G. Singh, S. Kim, A.V. Baskar, S. Joseph, J.-H. Yang, H. Ilbeygi, S.J.M. Ruban, V.T.H. Vu, A. Vinu, Microporous Mesoporous Mater. 267 (2018) 134–141.
[6] S. Joseph, D. Kempaiah, M. Benzigar, A.V. Baskar, S.N. Talapaneni, S.H. Jhung, D.-H. Park, A. Vinu, J. Mater. Chem. A 5 (2017) 21542–21549.
[7] M. Karthik, A. Tripathi, N. Gupta, A. Vinu, M. Hartmann, M. Palanichamy, V. Murugesan, Appl. Catal. A 268 (2004) 139–149.
[8] M. Miyahara, A. Vinu, K. Ariga, Mater. Sci. Eng. C 27 (2007) 232–236.
[9] P. Srinivasu, S. Alam, V.V. Balasubramanian, S. Velmathi, D.P. Sawant, W. Böhlmann, S.P. Mirajkar, K. Ariga, S.B. Halligudi, A. Vinu, Adv. Funct. Mater. 18 (2008) 640–651.
[10] E.S. Sanz-Pérez, T.C.M. Dantas, A. Arencibia, G. Calleja, A.P.M.A. Guedes, A.S. Araujo, R. Sanz, Chem. Eng. J. 308 (2017) 1021–1033.
[11] T. Joseph, S. Deshpande, S. Halligudi, A. Vinu, S. Ernst, M. Hartmann, J. Mol. Catal. Chem. 206 (2003) 13–21.
[12] K.S. Lakhi, W.S. Cha, J.-H. Choy, M. Al-Ejji, A.M. Abdullah, A.M. Al-Enizi, A. Vinu, Microporous Mesoporous Mater. 233 (2016) 44–52.
[13] K.S. Lakhi, A.V. Baskar, J.S.M. Zaidi, S.S. Al-Deyab, M. El-Newehy, J.-H. Choy, A. Vinu, RSC Adv. 5 (2015) 40183–40192.
[14] R.J. Perry, J.L. Davis, Energy Fuels 26 (2012) 2512–2517.
[15] Y. Kong, X. Shen, S. Cui, Microporous Mesoporous Mater. 236 (2016) 269–276.
[16] R. Ullah, M. Ali H Salah Saad, S. Aparicio, M. Atilhan, Microporous Mesoporous Mater. 262 (2018) 49–58.
[17] C. Robertson, R. Mokaya, Microporous Mesoporous Mater. 179 (2013) 151–156.
[18] A. Jain, R. Balasubramanian, M.P. Srinivasan, Chem. Eng. J. 283 (2016) 789–805.
[19] Z.Z. Chowdhury, M.R. Hasan, S.B. Abd Hamid, E. Marlina Samsudin, S.M. Zain, K. Khalid, RSC Adv. 5 (2015) 6345–6356.
[20] T. Wei, Q. Zhang, X. Wei, Y. Gao, H. Li, Sci. Rep. 6 (2016) 22646.
[21] M. Armandi, B. Bonelli, F. Geobaldo, E. Garrone, Microporous Mesoporous Mater. 132 (2010) 414–420.
[22] X. Han, L. Chu, S. Liu, T. Chen, C. Ding, J. Yan, L. Cui, G. Quan, BioResources 10 (2015) 2836–2849.
[23] G. Tan, W. Sun, Y. Xu, H. Wang, N. Xu, Bioresour. Technol. 211 (2016) 727–735.
[24] M. Vithanage, A. Rajapaksha, M. Zhang, S. Thiele-Bruhn, S. Lee, Y. Ok, Environ. Sci. Pollut. Res. 22 (2015) 2175–2186.
[25] X. Gu, Y. Wang, C. Lai, J. Qiu, S. Li, Y. Hou, W. Martens, N. Mahmood, S. Zhang, Nano Res. 8 (2015) 129–139.
[26] W. Sun, S.M. Lipka, C. Swartz, D. Williams, F. Yang, Carbon 103 (2016) 181–192.
[27] H.M. Coromina, D.A. Walsh, R. Mokaya, J. Mater. Chem. A 4 (2016) 280–289.
[28] J. Chen, J. Yang, G. Hu, X. Hu, Z. Li, S. Shen, M. Radosz, M. Fan, ACS Sustain. Chem. Eng. 4 (2016) 1439–1445.
[29] S.-M. Alatalo, K. Qiu, K. Preuss, A. Marinovic, M. Sevilla, M. Sillanpää, X. Guo, M.-M. Titirici, Carbon 96 (2016) 622–630.
[30] P. Regmi, J.L. Garcia Moscoso, S. Kumar, X. Cao, J. Mao, G. Schafran, J. Environ. Manag. 109 (2012) 61–69.
[31] W. Hao, E. Bjoerkman, Y. Yun, M. Lilliestrale, N. Hedin, ChemSusChem 7 (2014) 875–882.
[32] W.-J. Liu, H. Jiang, H.-Q. Yu, Chem. Rev. 115 (2015) 12251–12285.
[33] K.J. Sun, J.C. Tang, Y.Y. Gong, H.R. Zhang, Environ. Sci. Pollut. Res. 22 (2015) 16640–16651.
[34] M.C. Basso, A.L. Cukierman, Ind. Eng. Chem. Res. 44 (2005) 2091–2100.
[35] G. Singh, I.Y. Kim, K.S. Lakhi, P. Srivastava, R. Naidu, A. Vinu, Carbon 116 (2017) 448–455.
[36] G. Singh, K.S. Lakhi, I.Y. Kim, S. Kim, P. Srivastava, R. Naidu, A. Vinu, ACS Appl. Mater. Interfaces 9 (2017) 29782–29793.
[37] J. Deng, T. Xiong, F. Xu, M. Li, C. Han, Y. Gong, H. Wang, Y. Wang, Green Chem. 17 (2015) 4053–4060.
[38] Q. Niu, K. Gao, Q. Tang, L. Wang, L. Han, H. Fang, Y. Zhang, S. Wang, L. Wang, Carbon 123 (2017) 290–298.
[39] J. Han, J.H. Kwon, J.-W. Lee, J.H. Lee, K.C. Roh, Carbon 118 (2017) 431–437.
[40] Z. Wei, R. Pan, Y. Hou, Y. Yang, Y. Liu, Sci. Rep 5 (2015) 15664.
[41] A. Barroso-Bogeat, M. Alexandre-Franco, C. Fernández-González, V. Gómez-Serrano, Energy Fuels 28 (2014) 4096–4103.
[42] S. Hu, Y.-L. Hsieh, J. Mater. Chem. A 1 (2013) 11279–11288.
[43] S. Biniak, A. Świątkowski, M. Pakuła, M. Sankowska, K. Kuśmierek, G. Trykowski, Carbon 51 (2013) 301–312.
[44] Y. Önal, C. Akmil-Başar, Ç. Sarıcı-Özdemir, S. Erdoğan, J. Hazard Mater. 142 (2007) 138–143.
[45] S.M. Yakout, G. Sharaf El-Deen, Arb. J. Chem. 9 (2016) S1155–S1162.
[46] T. Du, J. Liang, N. Dong, L. Liu, L. Fang, S. Xiao, H. Han, Carbon 110 (2016) 278–285.
[47] Y. Cui, J.D. Atkinson, J. Mater. Chem. A 5 (2017) 16812–16821.
[48] G. Singh, I.Y. Kim, K.S. Lakhi, S. Joseph, P. Srivastava, R. Naidu, A. Vinu, J. Mater. Chem. A 5 (2017) 21196–21204.
[49] A. Anstey, S. Vivekanandhan, A. Rodriguez-Uribe, M. Misra, A.K. Mohanty, Sci. Total Environ. 550 (2016) 241–247.
[50] M.A. Lillo-Ródenas, D. Cazorla-Amorós, A. Linares-Solano, Carbon 41 (2003) 267–275.
[51] L. Kong, M. Su, Y. Peng, L.a. Hou, J. Liu, H. Li, Z. Diao, K. Shih, Y. Xiong, D. Chen, J. Clean. Prod. 168 (2017) 22–29.
[52] T. Wei, X. Wei, Y. Gao, H. Li, Electrochim. Acta 169 (2015) 186–194.
[53] P. Veerakumar, P. Thanasekaran, K.-C. Lin, S.-B. Liu, ACS Sustain. Chem. Eng. 5 (2017) 5302–5312.
[54] H. Zhong, C. Deng, Y. Qiu, L. Yao, H. Zhang, J. Mater. Chem. A 2 (2014) 17047–17057.
[55] J. Yu, M. Guo, F. Muhammad, A. Wang, F. Zhang, Q. Li, G. Zhu, Carbon 69 (2014) 502–514.
[56] P. Hao, Z. Zhao, Y. Leng, J. Tian, Y. Sang, R.I. Boughton, C.P. Wong, H. Liu, B. Yang, Nano Energy 15 (2015) 9–23.
[57] B. Li, F. Dai, Q. Xiao, L. Yang, J. Shen, C. Zhang, M. Cai, Adv. Energy Mater 6 (2016) 1600802.

[58] J.L. Hueso, J.P. Espinós, A. Caballero, J. Cotrino, A.R. González-Elipe, Carbon 45 (2007) 89–96.
[59] C. Zhang, W. Song, G. Sun, L. Xie, J. Wang, K. Li, C. Sun, H. Liu, C.E. Snape, T. Drage, Energy Fuels 27 (2013) 4818–4823.
[60] X. Li, Z.-Y. Sui, Y.-N. Sun, P.-W. Xiao, X.-Y. Wang, B.-H. Han, Microporous Mesoporous Mater. 257 (2018) 85–91.
[61] J. He, J.W.F. To, P.C. Psarras, H. Yan, T. Atkinson, R.T. Holmes, D. Nordlund, Z. Bao, J. Wilcox, Adv. Energy Mater 6 (2016) 1502491.
[62] G.K. Parshetti, S. Chowdhury, R. Balasubramanian, Fuel 148 (2015) 246–254.
[63] D.P. Vargas, L. Giraldo, J. Silvestre-Albero, J.C. Moreno-Piraján, Adsorption 17 (2011) 497–504.
[64] P. Deria, S. Li, H. Zhang, R.Q. Snurr, J.T. Hupp, O.K. Farha, Chem. Commun. (J. Chem. Soc. Sect. D) 51 (2015) 12478–12481.
[65] K.S. Lakhi, D.-H. Park, G. Singh, S.N. Talapaneni, U. Ravon, K. Al-Bahily, A. Vinu, J. Mater. Chem. A 5 (2017) 16220–16230.
[66] Z. Zhang, K. Wang, J.D. Atkinson, X. Yan, X. Li, M.J. Rood, Z. Yan, J. Hazard Mater. 229 (2012) 183–191.
[67] S. Cavenati, C.A. Grande, A.E. Rodrigues, J. Chem. Eng. Data 49 (2004) 1095–1101.
[68] A.R. Millward, O.M. Yaghi, J. Am. Chem. Soc. 127 (2005) 17998–17999.
[69] M.G. Singh, K.S. Lakhi, D.-H. Park, P. Srivastava, R. Naidu, A. Vinu, ChemNanoMat 4 (2018) 1–11.